Appl Magn Reson
DOI 10.1007/s00723-014-0593-8

Applied Magnetic Resonance

A Miniature Electron Spin Resonance Probehead for Transcutaneous Oxygen Monitoring

Helen Wolfson · Rizwan Ahmad · Ygal Twig · Periannan Kuppusamy · Aharon Blank

Received: 22 July 2014
© Springer-Verlag Wien 2014

Abstract Oxygen concentration in the skin is an important clinical indicator for monitoring pathological conditions such as chronic wounds, skin cancer, and peripheral vascular disease. Currently, the only clinically approved method for acquiring these oxygen levels is based on electrochemical measurements that employ Clarke-type electrodes attached to the skin. This technique has many drawbacks and limitations, making it unattractive for standard medical practice and care. Electron spin resonance (ESR), which can obtain the oxygen concentration through measurements of the spin–spin relaxation time (T_2) of paramagnetic species interacting with molecular oxygen, provides a possible alternative. However, a traditional ESR setup requires a large homogenous static magnetic field source with limited gap between the poles and complicated equipment, making it unattractive for clinical use. Here, we present a new design for a miniature ESR probehead, which is comprised of a specially designed permanent magnet and a small microwave resonator. The small size of the probehead (36 mm diameter cylinder with a height of 24 mm) enables transcutaneous measurements from virtually any part of the skin. Compared to the electrochemical method, this ESR-based approach may provide faster and more accurate readings of oxygen concentration in the skin, making it highly attractive for future clinical use.

H. Wolfson · Y. Twig · A. Blank (✉)
Schulich Faculty of Chemistry, Technion, Israel Institute of Technology, 32000 Haifa, Israel
e-mail: ab359@tx.technion.ac.il

R. Ahmad
Department of Electrical and Computer Engineering,
The Ohio State University, Columbus, OH 43210, USA

P. Kuppusamy
Departments of Radiology and Medicine, Geisel School of Medicine,
Dartmouth College, Lebanon, NH 03766, USA

Published online: 21 September 2014

1 Introduction

Tissue oxygen levels have significant importance in many clinical situations [1]. For instance, the role of hypoxia (lack of oxygen) in cancer treatment [2, 3], wound healing [4–6], and limb amputation [7] has been well documented. However, despite the great importance of oxygen, the clinical capability to noninvasively measure its concentration in the tissue has been limited. This is in contrast to measurement of blood oxygenation levels by methods such as pulse oximetry, which in many cases is not a good indicator of tissue oxygen levels [8]. The only noninvasive, clinically approved methodology for assessing oxygen levels in certain tissues is electrode-based transcutaneous oxygen monitoring (TCOM), which estimates skin tissue oxygenation by measuring the diffusion of extracellular oxygen through the skin [9, 10]. Currently, the TCOM electrode is used mainly for determining the healing capacity of wounds. However, it is employed in only $\sim$2 % of chronic wound cases. The main reasons for that are the complexity and inaccuracy of the method. Electrodes are clamped to the patient's skin via fixation rings and are heated to $\sim$43 °C. In some cases this process can cause first-degree burns to the patient, especially infants. After heating, the user performs oxygen measurements on the underlying tissue. The entire process can last from 45 to 90 min. These drawbacks, along with a high rate of user error (some experts estimate error to be as high as 60 % due to procedural complexity), lead to a low usage rate of this technology.

Electron spin resonance (ESR)-based methods are known to be very useful for quantifying oxygen concentration or oxygen partial pressure (pO_2). Such ESR measurements involve the use of an exogenous spin probe consisting of paramagnetic materials in either solid or soluble form. Changes in the relaxation times of the ESR spin probe (denoted as T_1 and T_2) are caused by the interaction of two paramagnetic species: molecular oxygen and the spin probe. These reversible oxygen-induced changes in the relaxation times are used to quantify the pO_2. Unlike BOLD magnetic resonance imaging (MRI) [11] and pulse oximetry [8], which measure blood oxygen saturation, ESR oximetry can measure the tissue oxygen directly. In the last 15 years, several sensitive, nontoxic, crystal-like oximetry spin probes have been developed [12–14]. The long-term stability of some of these probes in tissue environment has also been established [15, 16]. With respect to the TCOM applications, these particulates have recently been introduced in the form of a sticker (known as "SPOT Chip") that is permeable to oxygen only on its bottom surface [17]. This configuration allows the attainment of a fast O_2 equilibrium between the skin and the sticker placed on it. The relaxation times of the particulates in the sticker can, therefore, provide an accurate reading of the skin's pO_2. This technique makes it possible to implement TCOM applications by way of totally noninvasive measurements with a good temporal resolution.

Unfortunately, the use of such ESR-based techniques for clinical purposes still needs to address a number of fundamental issues, most notably the restrictions that arise from existing hardware limitations. As most conventional ESR systems are large, bulky units (somewhat reminiscent of MRI systems) with restrictive spacing between the magnet poles, refinements in ESR hardware are necessary to make this technology more appealing from a clinical standpoint. The movement towards

smaller, portable ESR systems would be of substantial benefit for both the end users (clinicians and clinical technicians) and the patients for whom such a system would be intended. As a smaller, portable system, the oximetry unit would be much more affordable and have the capability to be transported from room to room, rather than have the patient brought to a separate location. In critical care settings, this would be most useful because moving the patient is often not an option.

Over the last few years, we have developed several unique miniature magnetic resonance sensors that can operate locally without the need for a large external magnet. These sensors were already employed in a variety of clinical applications [18–20]. Here, we continue this trend and present a unique miniature ESR probehead that includes a permanent magnet and a high-sensitivity loop-gap resonator. This probehead can be paired with a special particulate spin probe to measure the oxygen concentration in the skin. This manuscript focuses on the technical aspects of the miniature ESR probehead: its design, characteristics, and specifications. The probe's clinical capabilities will be reported in future publications.

2 The Pulsed-ESR TCOM Probehead

2.1 Design Approach

The design goal was to produce a simple and compact probehead capable of effectively measuring the signal of particulate spin probes in the SPOT chip sticker placed on the skin, with sufficient sensitivity to provide accurate readings of the spin probe's T_2. Figure 1 shows the general overview of the probehead's conceptual design. The SPOT chip, which contains paramagnetic species such as LiNc-BuO used as a sensor of oxygen [21], is described in Fig. 2 (for further information see [17]). The $1/T_2$ of this spin probe grows linearly with the oxygen concentration [22], enabling the detection and quantification of transcutaneous oxygen diffusion

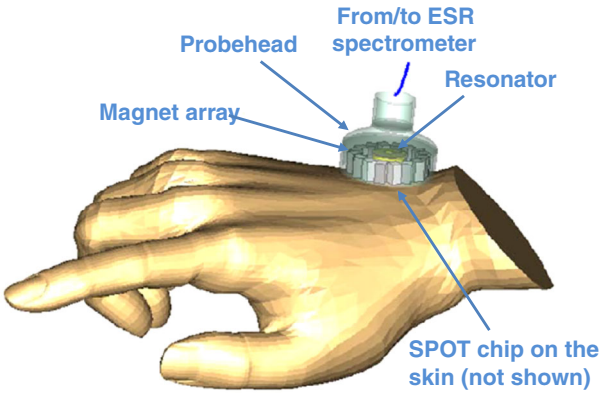

Fig. 1 General overview of the probehead showing the permanent magnet and resonator assembly during a projected in vivo measurement of skin oxygen level

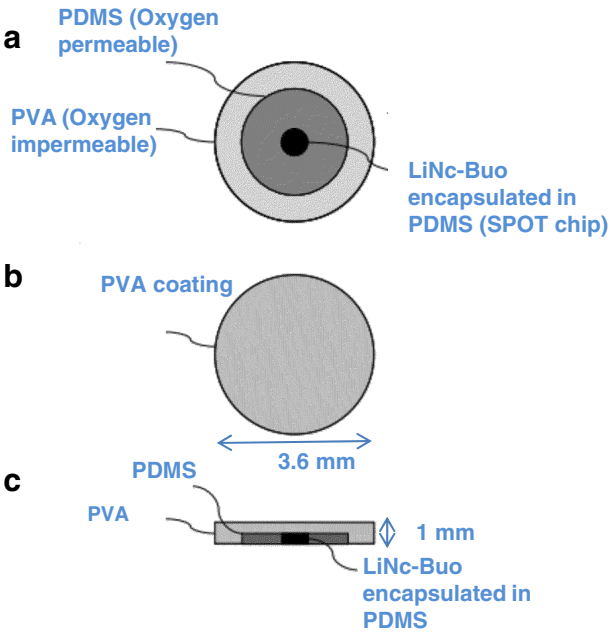

Fig. 2 Detailed illustration of a SPOT chip, made of the LiNc-BuO spin probe embedded in oxygen-permeable polydimethylsiloxane (PDMS), and encapsulated from the *top* by oxygen-impermeable polyvinyl alcohol (PVA). **a** View from the *bottom* of the chip. **b** View from the top of the chip. **c** Cross section of the SPOT chip

through the skin. In our case, the clinical measurements are to be carried out while the probehead is placed on the patient's skin, covering the SPOT chip sticker.

Our design features a static field of about 80 mT in the area occupied by the SPOT chip (about 1 mm above the skin), which translates into an ESR resonance frequency of $\sim$2.24 GHz, for which the skin's dielectric losses are not too significant. The measurement volume depends on the diameter of the TCOM probehead. The dimensions of the probehead are 36 diameter 24 mm height (Fig. 3), and its weight is $\sim$150 g, giving a measurement volume of $\sim$1.5 mm^3 (see Sect. 2.4). The probehead was designed in such a way that the resonator operates as an independent unit that can be used separately from the magnet. In this way, the performance of the system can be also evaluated in comparison to measurements performed with a conventional large homogenous ESR electromagnet.

2.2 The Magnet

The magnet is the most important and critical component of the probehead. To achieve our sensitivity goals, we chose to use a cylindrical Halbach array for the magnet design [23]. This kind of magnet structure can be built of separate magnet blocks, which are low-cost and lightweight, and provides a strong homogeneous static magnetic field along the transverse direction of the cylinder with low stray fields outside the structure. Halbach magnets have been previously studied both in

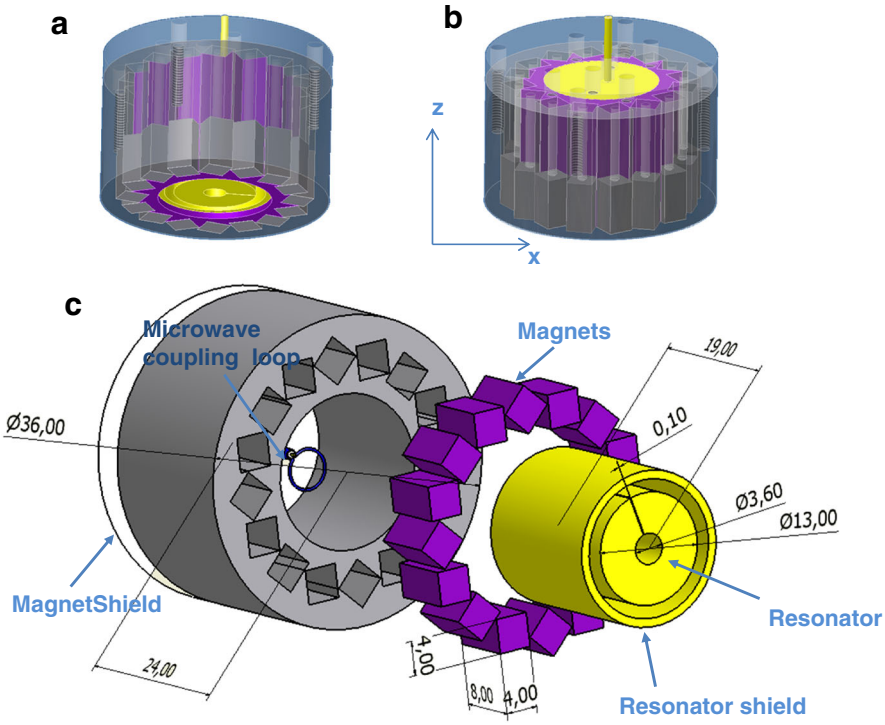

Fig. 3 Detailed view of the TCOM probehead assembly, showing it fully assembled (**a** and **b**) and also its individual components (**c**). All dimensions are in mm

NMR [24–29] and ESR [30]. However, a clinical use and a miniature design for ESR have not been suggested. The design and construction process of the magnet included a number of steps. First, we chose an appropriate magnet material. Second, the static field, B_0, was simulated using finite element analysis (Maxwell by Ansoft). Third, the magnetic design was optimized to maximize the ESR signal from the SPOT Chip.

The Halbach array is composed of a set of 16 permanent magnets shaped as 8-mm-long × 4-mm-wide × 4-mm-high rectangular prisms (Fig. 3). The magnets are made of Samarium Cobalt (SmCo, material # 2:17-TC16 from Electron Energy Corporation, USA) with a remanence of 0.83 T and a temperature coefficient of −10 ppm/°C. The array produces a weaker magnetic field than NdFeB rare-earth magnets, but provides far superior temperature stability.

The magnetization axis of each magnet runs parallel to one of the 4-mm dimensions. A metallic frame (made of nonmagnetic nickel–silver alloy) holds the magnets in a round array that is 24-mm long × 36-mm in diameter, in such a way that they are locked in position with their short sides at angles of 45° with respect to the frame (see Fig. 4a). This gives rise to a magnetic field B_0 perpendicular to the axis of the cylinder, as marked by a thick red arrow in Fig. 4a. The resonator is placed inside the magnet structure, with B_1 running perpendicular to B_0 along z-axis (Fig. 3b).

The static field vector, B_0, was measured using a 3D Hall probe (model 3RT100-2-2, Sentron, Zug, Switzerland) that has an integration volume of 100 × 100 × 100 μm, with 100-μm spatial resolution (Fig. 5a). Figure 5b shows the measured and calculated field along the z-axis of the probehead. The measured properties of the static field, B_0, closely follow the results obtained by the detailed finite element designs.

2.3 The Resonator

The resonator, its coupling structure, and microwave (MW) properties are presented in Fig. 6. It is a loop-gap ring resonator manufactured from solid copper. The

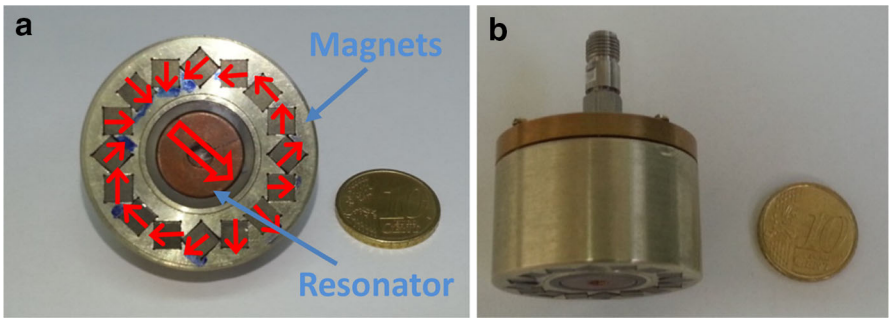

Fig. 4 Assembled probehead. **a** Picture of the assembled probehead showing the direction of the magnetization of the individual magnets (*small red arrows*) and the overall equivalent magnetization of the entire array (*large thick arrow*). The coin near the probehead is a 10-Euro-cents coin. **b** Picture of the assembled probe (lateral view)

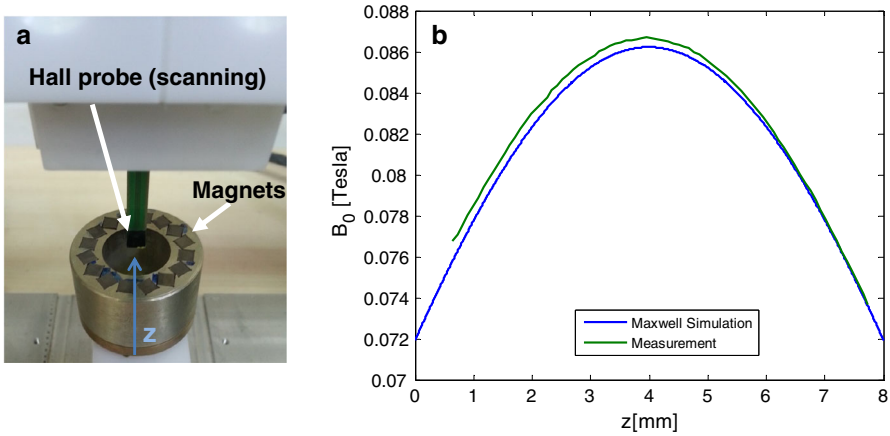

Fig. 5 Calculated and measured results of B_0 field mapping. **a** The setup for the magnetic field mapping. The Hall probe moves in space by step motors with a resolution of 100 μm. **b** The magnetic field along the z-axis, as calculated by the Maxwell simulation and measured by the Hall probe

resonator's dimensions are: outer diameter 13 mm, inner diameter 3.6 mm, height 19 mm, and the gap is 0.1 mm wide. The resonator is coupled to a coaxial transmission line by a loop antenna. The resonator design was carried out via finite element calculations (CST Microwave Studio, CST AG, Germany) so that its resonance frequency matches the static field of the permanent magnet (~2.3–2.5 GHz). The resonator is held in a Rexolite holder with a sapphire tuning element (model AT 6933-1 SL, Temex-Ceramics) inserted in the resonator gap that allows tuning its resonance frequency by ±100 MHz. The resonator's reflection coefficient (S_{11}) and quality factor were measured using a vector network analyzer (E8361A, Agilent Technologies, USA). The unloaded quality factor (Q_u) was found to be 200 in air environment, and it dropped to ~80 when brought close to the skin; see Fig. 6b. The quality factor is determined by the losses of the dielectric material we employed and mainly by radiation losses due to the open resonator structure. When brought close to the skin, the dielectric losses by the skin tissue also become significant. The effective resonator volume [31–34] (see also Sect. 4) was calculated from the finite element simulation results and was found to be 154 mm^3.

2.4 Optimizing the ESR Signal

The relatively small size of the magnet leads to inhomogeneous distributions of B_0, and the relatively small resonator results in an inhomogeneous MW magnetic field, B_1. As can be seen in Fig. 7a, these fields vary considerably in magnitude over the 3D region of interest (ROI). In addition, they also vary in their orientation. Therefore, for a given spatial distribution of B_0 and B_1, the net ESR signal must be calculated through the superposition of signals from individual spatial locations (called voxels) that may vary in amplitude and phase. This calculation was carried out using the Matlab software (Mathworks, Natick, MA, USA) that was introduced in our recent work on a compact ESR probehead for in vivo measurements of tooth

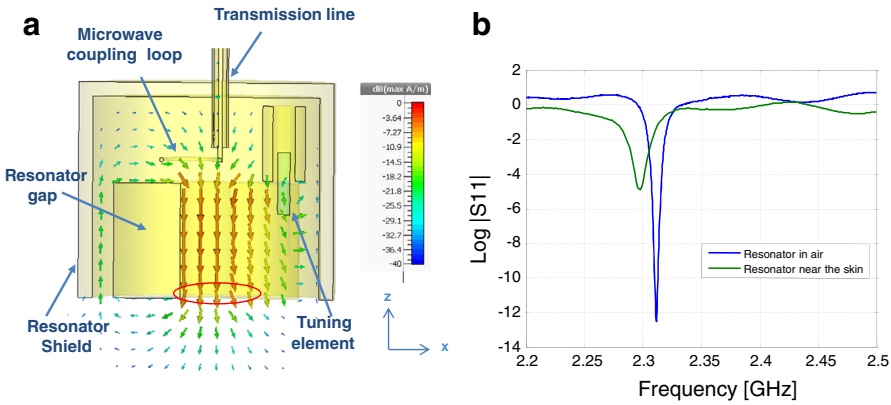

Fig. 6 Properties of the MW resonator. **a** Drawing of the calculated MW field of the resonator (B_1) superimposed on the cross section of the ring resonator. The *red circle* marks the region where the SPOT chip is to be placed. **b** Reflection coefficient, S_{11}, of the resonator in air and when brought near the skin

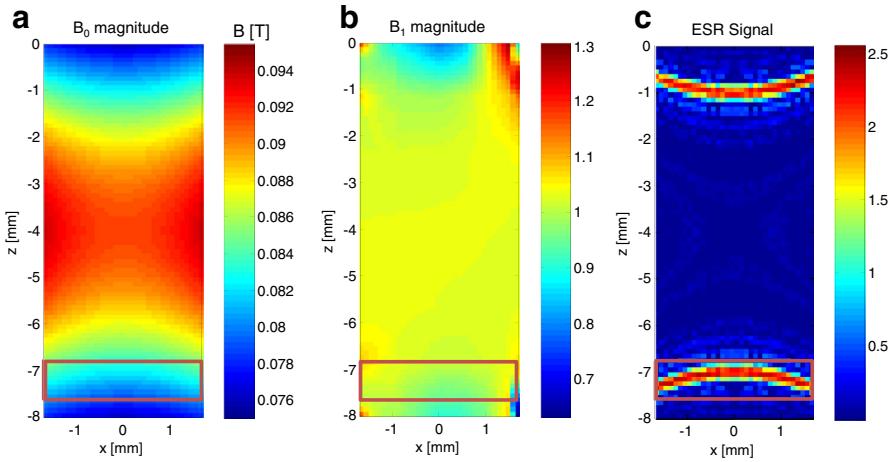

Fig. 7 Matlab simulation for estimating the spatial distribution of an ESR signal for given excitation frequency pulses, B_0 and B_1. The area in which the SPOT chip should be located is marked in all plots by a *red rectangle*. **a** B_0 magnitude as given by Maxwell Software at the probeheads' *xz* plane. **b** B_1 magnitude as given by CST software (arbitrary units) at the *xz* plane. **c** Matlab simulation showing the area from which the signal is obtained (in arbitrary units) at the *xz* plane, with the B_0 and B_1 values shown in (**a**) and (**b**). The excitation here is provided by a Hahn echo sequence with 100-ns-long *rectangular* pulses

[35]. The calculation is based on obtaining numerical solution of the Bloch equations for arbitrary values of B_0 and B_1 and for an arbitrary pulse excitation shape. Using the approximation of short (with respect to the transverse relaxation time) rectangular excitation pulses, a very efficient solution of the Bloch equations, e.g., using the method reported by Casanova and Perlo [36], can be obtained. Here, we set the frequency of the excitation pulses to be equal to the average value of γB_0 in the ROI (γ is the electro-geomagnetic ratio). The excitation bandwidth was controlled by adjusting the pulse width and/or shape, while the flip angle was controlled by adjusting the magnitude of a pulse. An example of the predicted ESR signal amplitude for a Hahn echo sequence employing rectangular pulses in various parts inside the probehead is provided in Fig. 7c.

2.5 Samples

Samples of the LiNc-BuO microcrystals in a tetragonal packing structure [37] were degassed and sealed under vacuum in a tube with an inner diameter of 1.56 mm. The spin relaxation times (T_1 and T_2), measured using inversion recovery and Hahn echo sequences, were found to be ~ 1 µs. The volume of the particulate powder in the sample was 3.6 mm^3 and the number of spins in the sample tube was found to be $\sim 1 \times 10^{17}$. The later datum was obtained by comparing the sample's signal to that of a trityl solution with known volume and concentration that was measured using a commercial CW ESR system (EMX X-band system by Bruker, Germany).

2.6 ESR Spectrometer

The MW system that drives the probehead is based on our home-built pulsed-ESR microimaging system. It includes a spectrometer, gradient current drivers (not used in the current set of experiments), and control software. A detailed description of the system is provided elsewhere [33, 38]. In experiments conducted in this work we extended the spectrometer's operating frequency range down to the 2–4 GHz range and also added the capability to perform arbitrary-shaped pulses using an arbitrary waveform generator card with 0.5 ns time resolution (Chase 12000 from Chase Scientific Company, USA).

3 Experimental Results

3.1 Evaluation of the Resonator's and the Spectrometer's Performance

The performance of the pulsed-ESR oximetry resonator was evaluated using the LiNc-BuO test sample. The sample was inserted into the loop-gap resonator and held in place using a tape, while the resonator was placed inside a homogeneous ESR electromagnet. The results of the frequency domain echo signal of these measurements and their corresponding noise levels are shown in Fig. 8. The experimental conditions were as follows: frequency of 2.24 GHz, Hahn echo pulse sequence employing Gaussian-shaped pulses, where the 90° pulse is 200 ns long (FWHM of 100 ns) and the 180° pulse is also 200 ns long (but with twice the amplitude), with interpulse separation, τ, of 800 ns. The repetition rate was 40 kHz and each echo signal was averaged 800 times (i.e., acquired within 20 ms). The noise was measured using the exact same parameters as the signal acquisition, but without any sample in the probehead. The experimental single-shot signal-to-noise ratio (SNR) values for these measurements are provided in Table 1 (see also Sect. 4 below for the theoretically calculated SNR). These values are derived by dividing the sample signal (integrated over its spectral width) with that of the noise signal (integrated over the same spectral window), acquired in a single shot.

3.2 Evaluation of the TCOM Probehead's Performance

The performance of the pulsed-ESR oximetry probehead was evaluated using the same set of parameters as above, with the homogenous static field replaced by the field of the Halbach array (that is, the complete probehead was used). The LiNc-BuO crystals in the capillary were placed inside the loop-gap resonator, mimicking the position of the SPOT chip. The experimental conditions were the same as above. The noise in this case was measured by collecting the signal after removing the sample. The frequency domain echo signal of the LiNc-BuO sample compared to the noise is plotted in Fig. 8, with 800 averages. The experimental single-shot SNR values for these test sample measurements are provided in Table 1.

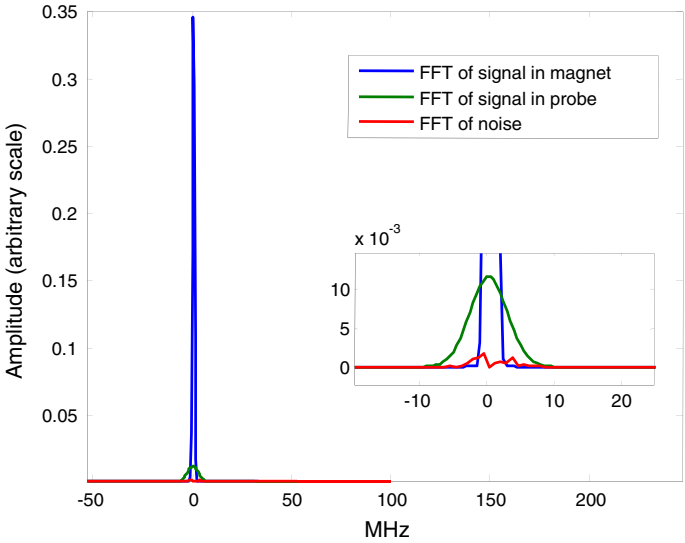

Fig. 8 Signal and noise levels (in arbitrary units) measured by the probehead for the LiNc-BuO sample (shown in the frequency domain relative to central frequency). The *inset* shows a blow up of the noise level

Table 1 Theoretical and experimental single-shot SNR of both the probe measurement and magnet measurement

	LiNc-BuO in Hom. Magnet	LiNc-BuO in probe
Experimental SNR	15.4	2.5
Theoretical SNR	550 (whole sample)	10

The theoretical values were calculated using Eq. 1

4 Discussion

The results clearly show that a sample with the typical size of the SPOT chip provides sufficient SNR in a fraction of a second ($\sim$20 ms). Clinical measurements would require having several signal acquisitions at various values of τ. In addition, SNR may be lower due to a reduction in Q when the probe is near the skin and to other possible experimental issues. These effects may result in a significant increase in the acquisition time required to obtain accurate pO_2 readings. However, we expect the acquisition time to stay below 5 s. This is because, if required, the acquisition protocol can be further optimized by increasing the repetition rate to few 100 kHz, which can further reduce the acquisition time.

The following theoretical SNR analysis compares the performance of the probehead to the expected sensitivity.

The number of spins detectable with an SNR of 1 in a single-shot data acquisition is given by the expression [34]:

$$\text{Sensitivity}_{\text{single shot}}^{\text{spins}} \approx \frac{8\sqrt{V_c}\sqrt{k_b T(1/\pi T_2^*)}}{\mu_B \omega_0 \sqrt{2\mu_0}} \sqrt{\frac{\omega_0}{Q_u}} B_F, \quad (1)$$

where V_c is a property of the resonator that represents its effective volume [31–34], which is equal to the volume of a small hypothetical sample V_v [for example, $(1\ \mu m)^3$] at the center of the resonator's field of view, divided by the filling factor [39] of this small sample [31]. Other parameters in the equation are: Boltzmann constant, k_b, temperature, T, the electron's Larmor angular frequency, ω_0, the free-space permeability, μ_0, and the unloaded quality factor of the resonator, Q_u. Here we assumed that the bandwidth of excitation is chosen to match the line width of the paramagnetic species in the sample, $\Delta f = 1/\pi T_2^*$ (including any broadening due to B_0 inhomogeneity). B_F is the Boltzmann population factor, $B_F = \frac{1+e^{-\frac{\hbar\omega_0}{k_B T}}}{1-e^{-\frac{\hbar\omega_0}{k_B T}}}$, and μ_B is Bohr's magneton.

Plugging the relevant parameters for the LiNc-BuO sample in the homogenous magnet into Eq. 1 (i.e., $T_2^* = 1{,}000$ ns, $B_F = 5.43 \times 10^3$, $V_c = 1.54 \times 10^{-7}$ m^3, $Q_u = 200$, and $\omega_0 = 1.44 \times 10^{10}$ rad/s) provides us with a theoretical single-shot spin sensitivity of $\sim 2.44 \times 10^{13}$ spins for this sample. This means that our 1×10^{17}-spin LiNc-BuO sample, if wholly excited, should have given a single-shot SNR of $\sim 1 \times 10^{17}/2.44 \times 10^{13} = 4{,}000$. However, we must also consider the T_2 relaxation, which, for our Hahn echo sequence, reduces the signal by a factor of ~ 7.4, leaving us with a predicted single-shot SNR of $\sim 4{,}000/7.4 = 550$. The theoretical SNR inside the small permanent magnet of the probe can be calculated in a similar manner. However, the volume from which the signal is picked up is ~ 15 times smaller than that of the entire sample (based on the analysis of Fig. 7). Furthermore, the field inhomogeneity causes T_2^* to be much smaller (~ 80 ns), resulting in a predicted single-shot SNR of ~ 10 (which already takes into consideration the effect of the T_2 relaxation of the ESR signal).

An inspection of the data in Table 1 reveals that the resulting theoretical sensitivity values are significantly better than those actually obtained in the experiments. These differences may occur due to uncertainties in the number of spins in the sample and to the sample's non-ideal pulse sequence excitation when placed in a resonator with relatively large B_1 field variations. Also, some variability that we observed in the measured-ESR signal can be attributed to the positioning of the sample inside the resonator. An ideal measurement would be approximately at $z = 4$ mm (Fig. 7), where the B_0 and B_1 fields are relatively homogeneous. However, due to the technical reasons of SPOT chip size and placement, the measurement can only be carried out in the inhomogeneous region that is close to the surface of the resonator, leading to some loss of ESR signal. The relatively larger difference between the theoretical and experimental SNR values in the homogenous magnet case is due to limited dynamic range of the MW system that forced us to work at relatively low gain in this case, which increases the system's noise figure.

The combination of the ESR probehead and SPOT chip not only provides a viable alternative to electrode-based measurements of transcutaneous oxygen but also offers several advantages. The fast acquisition by probehead and the small size

of the SPOT chip, which leads to a rapid equilibrium with the skin, would possibly allow the entire measurement process to be significantly faster compared to electrode-based acquisition. It would also possibly not need heating of the skin because of the much better diffusion of oxygen to the paramagnetic crystallite spin probe (that can be in gaseous environment) vs. the relatively slow diffusion in the electrolyte solution of the TCOM electrode. There is no oxygen consumption during the measurement, and the patch can be attached directly to a wound surface and also to very small pointy organs. Furthermore, in the future, the system can be adapted for subcutaneous applications where the probehead pickups signal from the paramagnetic species deposited just underneath the epidermis. In addition, by reducing the size of the rest of the spectrometer system, it is possible to design an entire system that is portable and can be transported on a cart. Future work, together with clinical studies with an actual SPOT chip, may concentrate on improving the sensitivity and usability of such an oximetry probe.

Acknowledgments This work was supported by funding from the NIH (1R21 EB016189-01) and by grant no. 201665 from the European Research Council (ERC).

References

1. R.D. Restrepo, K.R. Hirst, L. Wittnebel, R. Wettstein, Respir. Care **57**, 1955–1962 (2012)
2. M. Hockel, K. Schlenger, M. Mitze, U. Schaffer, P. Vaupel, Semin. Radiat. Oncol. **6**, 3–9 (1996)
3. H.M. Swartz, B.B. Williams, R.J. Nicolalde, E. Demidenko, A.B. Flood, Radiat. Meas. **46**, 742–748 (2011)
4. G.M. Gordillo, R. Schlanger, W.A. Wallace, V. Bergdall, R. Bartlett, C.K. Sen, Oxyg. Sens. **381**, 575–585 (2004)
5. H.W. Hopf, J.J. Gibson, A.P. Angeles, J.S. Constant, J.J. Feng, M.D. Rollins, M.Z. Hussain, T.K. Hunt, Wound. Repair. Regen. **13**, 558–564 (2005)
6. R. Ogrin, M. Woodward, G. Sussman, Z. Khalil, Int. Wound. J. **8**, 437–445 (2011)
7. K.A. Arsenault, A. Al-Otaibi, P.J. Devereaux, K. Thorlund, J.G. Tittley, R.P. Whitlock, Eur. J. Vasc. Endovasc. Surg. **43**, 329–336 (2012)
8. R.J. Kopotic, Anesth. Analg. **105**, S103–S105 (2007)
9. A.A. Saber, K.Z. Yahya, A. Rao, M. Castellano, M. Cioroiu, R. Grossi, R.M. Tornambe, J. Invest. Surg. **18**, 321–323 (2005)
10. R.E. Grolman, D.K. Wilkerson, J. Taylor, P. Allinson, M.A. Zatina, Am. Surg. **67**, 1072–1079 (2001)
11. S. Ogawa, T.M. Lee, A.R. Kay, D.W. Tank, Proc. Natl. Acad. Sci. USA **87**, 9868–9872 (1990)
12. G. Ilangovan, J.L. Zweier, P. Kuppusamy, J. Magn. Reson. **170**, 42–48 (2004)
13. R.P. Pandian, N.L. Parinandi, G. Ilangovan, J.L. Zweier, P. Kuppusamy, Free Radic. Biol. Med. **35**, 1138–1148 (2003)
14. M. Afeworki, N.R. Miller, N. Devasahayam, J. Cook, J.B. Mitchell, S. Subramanian, M.C. Krishna, Free Radic. Biol. Med. **25**, 72–78 (1998)
15. N. Khan, H.G. Hou, P. Hein, R.J. Comi, J.C. Buckey, O. Grinberg, I. Salikhov, S.Y. Lu, H. Wallach, H.M. Swartz, Oxyg. Transp. Tissue Xxvi. **566**, 119–125 (2005)
16. M. Khan, V.K. Kutala, S. Wisel, S.M. Chacko, M.L. Kuppusamy, P. Kwiatkowski, P. Kuppusamy, Oxyg. Transp. Tissue Xxix. **614**, 45–52 (2008)
17. E. Eteshola, P. Kuppusamy, G. Meenakshisundaram, B. Rivera, in *Devices and methods for measuring oxygen*, ed. by T.O.S.U.R. Foundation, US patent application US20120296188 (2012)
18. A. Blank, G. Alexandrowicz, L. Muchnik, G. Tidhar, J. Schneiderman, R. Virmani, E. Golan, Magn. Reson. Med. **54**, 105–112 (2005)
19. A. Blank, S. Ish-Shalom, L. Shtirberg, Y. Zur, Magn. Reson. Med. **62**, 1585–1596 (2009)
20. K. Sirota, Y. Twig, A. Blank, Appl. Magn. Reson. **44**, 671–689 (2013)

21. R.P. Pandian, M. Dolgos, C. Marginean, P.M. Woodward, P.C. Hammel, P.T. Manoharan, P. Kuppusamy, J. Mater. Chem. **19**, 4138–4147 (2009)
22. R.P. Pandian, Y.I. Kim, P.M. Woodward, J.L. Zweier, P.T. Manoharan, P. Kuppusamy, J. Mater. Chem. **16**, 3609–3618 (2006)
23. K. Halbach, Nucl. Instrum. Methods **169**, 1–10 (1980)
24. C.W. Windt, H. Soltner, Dv Dusschoten, P. Blümler, J. Magn. Reson. **208**, 27–33 (2011)
25. B.P. Hills, K.M. Wright, D.G. Gillies, J. Magn. Reson. **175**, 336–339 (2005)
26. H. Raich, P. Blümler, Concepts Magn. Reson. Part B. Magn. Reson. Eng. **23B**, 16–25 (2004)
27. W.H. Chang, J.H. Chen, L.P. Hwang, Magn. Reson. Imaging **24**, 1095–1102 (2006)
28. S. Anferova, V. Anferov, D.G. Rata, B. Blümich, J. Arnold, C. Clauser, P. Blümler, H. Raich, Concepts Magn. Reson. Part B. Magn. Reson. Eng. **23B**, 26–32 (2004)
29. G. Moresi, R. Magin, Concepts Magn. Reson. Part B. Magn. Reson. Eng. **19B**, 35–43 (2003)
30. C. Bauer, H. Raich, G. Jeschke, P. Blumler, J. Magn. Reson. **198**, 222–227 (2009)
31. A. Blank, C.R. Dunnam, P.P. Borbat, J.H. Freed, J. Magn. Reson. **165**, 116–127 (2003)
32. A. Blank, J.H. Freed, Isr. J. Chem. **46**, 423–438 (2006)
33. A. Blank, E. Suhovoy, R. Halevy, L. Shtirberg, W. Harneit, Phys. Chem. Chem. Phys. **11**, 6689–6699 (2009)
34. Y. Twig, E. Suhovoy, A. Blank, Rev. Sci. Instrum. **81**, 104703 (2010)
35. W. Helen, A. Rizwan, T. Ygal, W. Benjamin, B. Aharon, Health. Phys. (2014) (in press)
36. F. Casanova, J. Perlo, in *Single-Sided NMR*, ed. by F. Casanova, J. Perlo, B. Blümich (Springer, Berlin Heidelberg, 2011), pp. 11–56
37. R.P. Pandian, N.P. Raju, J.C. Gallucci, P.M. Woodward, A.J. Epstein, P. Kuppusamy, Chem. Mater. **22**, 6254–6262 (2010)
38. L. Shtirberg, Y. Twig, E. Dikarov, R. Halevy, M. Levit, A. Blank, Rev. Sci. Instrum. **82**, 043708 (2011)
39. C.P. Poole, *Electron Spin Resonance : a Comprehensive Treatise on Experimental Techniques* (Wiley, New York, 1983)